Proceedings of International Structural Engineering and Construction, 12(1), 2025
Integrating Technology for Advanced Practices in Structural Engineering and Construction
Edited by Vimonsatit, V., Askarinejad, H., Pour, M., Singh, A., and Yazdani, S.

www.doi.org/10.14455/ISEC.2025.12(1).STR-65

FLEXURAL RESPONSE OF FRP BONDED AUTOCLAVED AERATED CONCRETE BEAMS

ERTURK TUNCER[1], BARIS BINICI[2], and ERDEM CANBAY[2]

[1]*Dept of Civil Engineering, TED Univ, Ankara, Turkey*
[2]*Dept of Civil Engineering, Middle East Technical Univ, Ankara, Turkey*

Fiber Reinforced Polymers (FRPs) are widely recognized for their advantages including low weight, high tensile strength, and resistance to corrosion. This study aims to investigate the structural behavior of Autoclaved Aerated Concrete (AAC) beams that are strengthened with externally bonded FRP laminates. An experimental program was carried out using unidirectional carbon fiber laminates placed in single layers, either partially (half-width) or fully covering top and bottom faces of the beams. The experimental results were analyzed in terms of stiffness, ultimate strength, and ductility. In addition to experimental work, a numerical study was performed using both section analysis and nonlinear finite element modeling (FEM) to predict the load-deformation behavior of the specimens. The effective FRP strain values obtained from the analyses were also compared with the provisions of ACI 440.2R. Findings indicate that a reduction factor of approximately 60% should be applied to the effective FRP strain when designing FRP-strengthened AAC beams.

Keywords: Fiber bonding, Finite element simulation, Ductility, Effective debonding strain.

1 INTRODUCTION

Autoclaved Aerated Concrete (AAC) is preferred in construction due to its lightweight nature, excellent fire-resistance, superior thermal and acoustic insulation, long-term durability, and ease of installation. Typical applications of AAC include infill walls, reinforced panels, and beams used in roofs, floors, and lintels. In recent years, numerous studies have been conducted to understand the behavior of reinforced concrete (RC) frames infilled with AAC blocks. For instance, Huang *et al*. (2012) implemented laboratory tests to discover the performance of AAC-infilled RC frames under in-plane cyclic loading. Schwarz *et al*. (2015) examined the influence of wall openings, prestressing, and wall aspect ratios on AAC-infilled RC frames through a series of cyclic tests. Milanesi *et al*. (2018) focused on the deformation limits of AAC-infilled frames, specifically analyzing the impact of the presence of sliding joints. In addition to infilling walls, AAC wall panels have been studied by several researchers to assess their applicability in seismic zones (Tanner *et al*. 2005, Varela *et al*. 2006, Costa *et al*. 2011). Apart from those, the existing literature involves only a limited number of studies addressing the behavior of FRP-bonded AAC beams. For example, carbon fiber-reinforced polymer (CFRP) and glass fiber-reinforced polymer (GFRP) bonded AAC beams were tested using flexural and shear wrapping techniques to demonstrate the sufficient structural performance of such elements (Mousa and Uddin 2009, Memari *et al*. 2010). Based on the literature review, the objectives of this study are as follows: (1) to experimentally examine the behavior of AAC elements strengthened with externally bonded FRP laminates, (2) to

validate analytical section-based analysis and finite element modeling (FEM) through laboratory tests, and (3) to predict the effective FRP strain values for potential application in the structural design of AAC members.

2 LABORATORY TESTS

Four-point bending tests were implemented for all specimens. Table 1 introduces the material properties of steel and CFRP. In addition to those, the characteristic compressive strengths of AAC are 2.5 MPa and 3.5 MPa for the steel-reinforced and CFRP-bonded AAC beams, respectively. In the scope of this research, a total of nine specimens were tested. All specimens had a constant cross-sectional height of 250 mm, while their widths were either 100 mm or 200 mm. Unidirectional CFRP laminates were externally bonded to both top and bottom surfaces along the full length of beam. The laminates were applied either partially (half of the specimen width) or fully (full of the specimen width). In addition to FRP-bonded beams, three specimens were solely reinforced with steel bars. Based on the reinforcement type and specimen dimensions, the beams were categorized into three groups. Group I consists of steel-reinforced specimens. Groups II and III include CFRP-bonded specimens with cross-sectional dimensions of 100 mm × 250 mm and 200 mm × 250 mm, respectively. A systematic nomenclature was developed for specimen labeling. Accordingly, the first letter indicates the reinforcement type: "S" denotes the reference steel-reinforced specimens, whereas "C" represents the composite beams strengthened by CFRP. The fiber usage is also designated by this letter: "F" and "H" refer to full-width and half-width application, respectively. For example, "FC" implies a specimen with full-width CFRP bonding, whereas "HC" indicates half-width CFRP bonding. The second letter defines the shear span length, and the third indicates the specimen width. All dimensions specified in these identifiers are given in centimeters.

Table 1. Material properties.

Material type	Yield strength (MPa)	Elasticity modulus (MPa)	Ultimate tensile strength (MPa)	Ultimate tensile strain (mm/mm)
Steel	495	200000	640	0.120
CFRP	-	260000	3900	0.015

The load-deformation responses of the test beams are presented in Figure 1. A summary of experimental results is also provided in Table 2. Accordingly, several structural parameters such as secant stiffness (K), ultimate load (V_u), yield displacement (Δ_y), ultimate displacement (Δ_u), and displacement ductility (μ_Δ) were obtained to make a comparison between steel-reinforced and CFRP-bonded beams. In the same table, V_{flex} is the shear force obtained from bending moment capacity of the section. V_{shear} indicates the shear capacity of the section. As expressed in Eq. (1), the shear capacity of AAC beam was computed in accordance with ACI 526R (ACI Committee 526 2019) guidelines. In this equation, f_{AAC} represents the compressive strength of AAC. Section width and effective depth are denoted as b_w and d, respectively. Due to the absence of transverse reinforcement and the shear-oriented application of FRP laminates, the shear resistance was assumed to be provided solely by the AAC (V_{AAC}).

$$V_{AAC} = 0.066\sqrt{f_{AAC}}b_w d \quad (1)$$

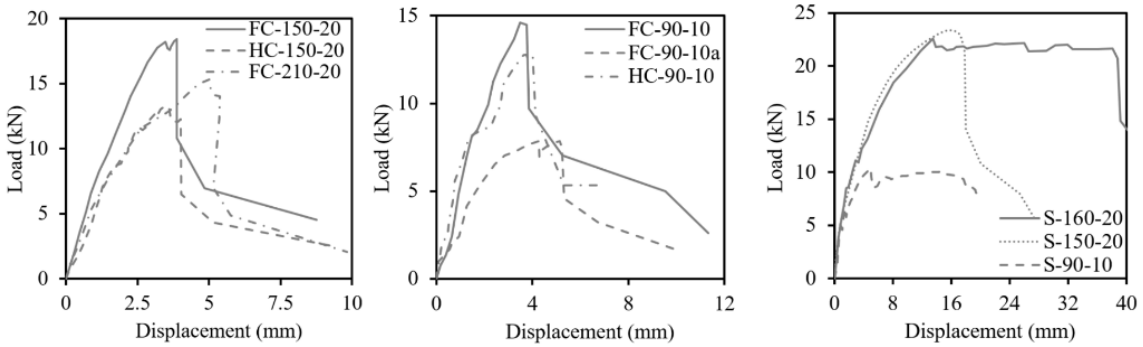

Figure 1. Load-displacement curves of test specimens.

Table 2. Test results.

Specimen	Δ_y (mm)	Δ_u (mm)	K (kN/m)	μ_Δ	V_u (kN)	V_{flex} (kN)	V_{shear} (kN)
S-90-10	3.1	5.2	3297	1.7	10.4	11.5	7.0
S-150-20	8.0	17.9	2914	2.2	23.4	19.7	14.0
S-160-20	8.6	38.9	2615	4.5	22.1	18.5	14.0
FC-90-10	3.1	3.8	4651	1.2	14.6	26.4	2.6
FC-90-10a	2.7	5.3	2896	1.9	7.9	26.4	2.6
HC-90-10	3.4	4.1	3784	1.2	12.8	13.3	2.6
FC-210-20	3.4	5.4	4541	1.6	15.3	22.6	5.2
FC-150-20	3.7	3.9	4914	1.0	18.4	31.7	5.2
HC-150-20	2.9	4.0	4606	1.4	13.3	15.9	5.2

(*) Except for FC-90-10a, all composite test specimens were bonded using an epoxy-based adhesive. FC-90-10a was the only specimen for which an AAC adhesive was applied.

2.1 Group I

All beams failed due to the formation of flexural crack. Among the test specimens with cross-sectional dimensions of 100 mm × 250 mm and 200 mm × 250 mm, the highest load capacities were recorded for S-90-10 and S-150-20, respectively. Nevertheless, S-160-20 exhibited the greatest displacement ductility. Although the load-carrying capacities of S-150-20 and S-160-20 were nearly identical, the displacement ductility of S-160-20 was approximately twice that of S-150-20. This discrepancy might be attributed to the difference in failure mechanisms: A bonding failure between AAC and reinforcing steel occurred for S-150-20, whereas S-160-20 demonstrated a ductile response characterized by steel yielding followed by AAC crushing. Additionally, Table 2 indicates that S-90-10 had the highest secant stiffness. Such a situation might be associated with its relatively low mild steel ratio compared to the other specimens.

2.2 Group II

As presented in Table 2, the specimen FC-90-10 exhibited approximately 25% higher secant stiffness compared to HC-90-10 despite containing twice the amount of fiber. The primary difference between FC-90-10 and FC-90-10a was the type of bonding material employed. Specifically, FC-90-10 utilized an epoxy-based adhesive, resulting in a stiffer response compared to the FRP system bonded with AAC adhesive in FC-90-10a. Both FC-90-10 and HC-90-10 experienced flexural shear cracks followed by FRP debonding, ultimately failing in a brittle manner. Conversely, FC-90-10a showed a combination of flexural shear cracking, AAC crushing, and FRP debonding. As a result, a more ductile response was obtained for FC-90-10a.

Furthermore, the load-carrying capacity of FC-90-10 was nearly twice that of FC-90-10a, which can be explained by the variations in mechanical properties between the epoxy adhesive and the AAC-based bonding agent.

2.3 Group III

As can be seen from Figure 1, the specimen FC-150-20 exhibited approximately 40% greater load capacity than HC-150-20, primarily due to the application of twice the amount of FRP. On the other hand, both specimens had similar higher secant stiffness values. The shear cracking developed in the specimen with full-width FRP coverage, whereas FRP delamination was observed in the specimen with half-width FRP application. Owing to the brittle nature of FRP, the smaller amount of fiber enabled to exhibit more ductile response (FC-150-20 vs. HC-150-20). The highest displacement ductility was observed in FC-210-20 because its ultimate deformation capacity was greater than the others. This case might be explained by its longer span providing a more uniform load distribution and failure pattern.

3 DISCUSSIONS OF RESULTS

The assessment of specimens S-150-20 and FC-150-20 reveals that FRP-bonded members can be designed to achieve adequate load-carrying capacity despite their relatively low ductility levels. Similarly, the approximately 50% higher load capacity of FC-90-10 compared to S-90-10 highlights the potential of FRP bonding in enhancing strength. Besides, FRP bonding significantly improved the stiffness of the beams. For example, specimens FC-150-20 and FC-90-10 had higher secant stiffness values than corresponding reference beams with identical cross-sectional dimensions and span lengths. This enhanced stiffness offers a notable advantage in controlling deflections under service loads. The predominant failure types observed in the FRP-bonded AAC beams were shear and FRP debonding. These modes were due to the use of FRP laminates positioned on both tension and compression faces. As a result of this fiber layout, flexural moment capacity was substantially improved, then, the composite specimens were susceptible to sheer failure. On the contrary, steel-reinforced beams showed flexure-based failure mechanisms. Apart from those, Table 2 reveals that ultimate loads measured throughout the laboratory tests exceeded the shear capacities dictated by ACI 526R (ACI Committee 526 2019). For the composite specimens, the peak loads were within the range of the shear and flexural shear capacities. It is also evident that using ultimate FRP strain values in moment capacity calculations may result in significant overestimation of flexural strength.

4 MODELING

4.1 Section Analysis

Based on ultimate limit state assumptions, moment-curvature responses were derived for all composite AAC beams. Then, load-displacement curves were obtained. Figure 2 introduces the comparison of load-displacement relation between laboratory study (solid line) and section analysis (dashed line). Accordingly, it can be said that a reasonable agreement was achieved for all CFRP-bonded test specimens. The analyses were performed until the specimens reached their ultimate load capacities measured during the experiments. The strain level at this point is named as effective debonding strain (ε *). For comparative purposes, Eq. (2) proposed by ACI 440.2R (ACI Committee 440 2017) was also employed. In this formulation, the debonding strain of the fiber (ε_{fd}) depends on the following parameters: Fiber thickness (t_{frp}), the number of fiber layers (n_{frp}), the concrete compressive strength (f_c'), and the elasticity modulus of the fiber (E_{frp}). Additionally,

it is noted that the calculated strain level must not exceed 0.9 times the ultimate strain of the fiber (ε_{fu}).

$$\varepsilon_{fd} = 0.41 \cdot \sqrt{\frac{f_c'}{n_{frp} \cdot t_{frp} \cdot E_{frp}}} \leq 0.9\varepsilon_{fu} \quad (2)$$

4.2 Nonlinear Finite Element Simulation

FRP bonded AAC beams were modeled using four-node plain stress elements. Elastic truss elements were employed for FRPs. The model developed by Darwin and Pecknold (1977) was adopted for the compression response of AAC. Despite the extremely low tensile strength of AAC, a linear softening path was considered for modeling purposes. A displacement-controlled loading protocol was carried out up to the maximum load points. Figure 3 illustrates the load-displacement comparison of experimental and computer model results. Accordingly, similar curve trends were observed, therefore, it can be said that finite element model simulations well predicted the laboratory findings. The strain levels at the ultimate loads were determined. Furthermore, effective debonding strains calculated with the help of section analyses and nonlinear finite element simulations are presented in Table 3. This table indicates that the strains determined through both approaches were remarkably similar. Further details of this research are also available in the study conducted by Tuncer *et al*. (2021).

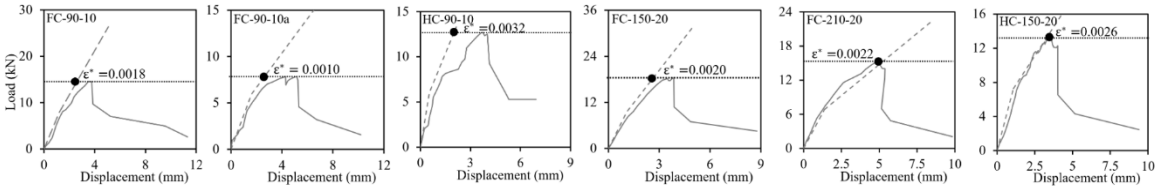

Figure 2. Load vs. displacement between section analysis and experimental work.

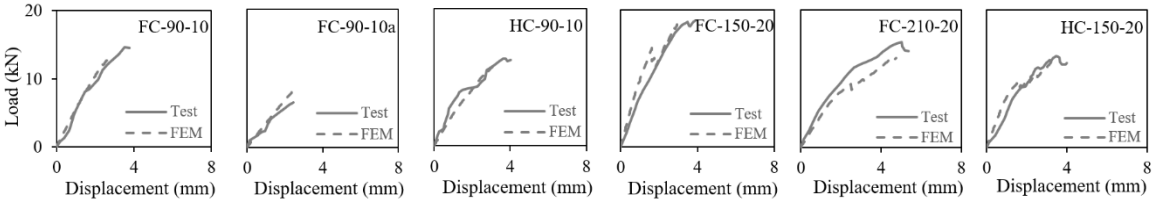

Figure 3. Load vs. displacement between test and finite element analysis.

Table 3. Effective debonding strain values.

Specimen	Section analysis	Finite element	Design proposal	ACI proposal
FC-90-10	0.0018	0.0016	0.0020	0.0033
FC-90-10a	0.0010	0.0014		
FC-150-20	0.0020	0.0018		
FC-210-20	0.0022	0.0019		
HC-90-10	0.0032	0.0026	0.0025	0.0033
HC-150-20	0.0026	0.0024		

5 CONCLUSIONS

In this research, a total of nine autoclaved aerated concrete (AAC) beams were experimentally examined under four-point bending tests to analyze their secant stiffness, ultimate strength, and ductility. Additionally, a numerical study of load–displacement responses was conducted for the comparison with the experimental findings. The key conclusions derived from this limited experimental program are summarized as follows:

(1) FRP-bonded AAC beams might be designed to achieve ultimate load-carrying capacities comparable to those of steel-reinforced counterparts whereas maintaining adequate stiffness to satisfy serviceability criteria. However, these beams generally exhibit limited ductility.
(2) Load-displacement responses estimated through simplified section analyses and finite element simulations showed satisfactory agreement with experimental results.
(3) The debonding strain provision of ACI 440.2R was found to lead to unconservative designs. Based on experimental observations, analytical studies, and numerical modeling, it is suggested that 60% of the effective strain value specified in ACI 440.2R may be appropriate for the FRP design of AAC members.

References

ACI Committee 440, *ACI 440.2R-17: Guide for the Design and Construction of Externally Bonded FRP Systems for Strengthening Concrete Structures*, American Concrete Institute (ACI), Farmington Hills, MI, May, 2017.

ACI Committee 526, *ACI 526R-19: Guide for Design and Construction with Autoclaved Aerated Concrete Panels*, American Concrete Institute (ACI), Farmington Hills, MI, July, 2019.

Costa, A. A., Penna, A., and Magenes, G., *Seismic Performance of Autoclaved Aerated Concrete (AAC) Masonry: From Experimental Testing of the In-Plane Capacity of Walls to Building Response Simulation*, Journal of Earthquake Engineering, Taylor & Francis, 15(1), 1–31, January 2011.

Darwin, D., and Pecknold, D. A., *Nonlinear Biaxial Stress-Strain Law for Concrete*, Journal of the Engineering Mechanics Division, ASCE, 103(2), 229–241, April 1977.

Huang, X. Y., Ni, W., Cui, W. H., Wang, Z. J., and Zhu, L. P., *Preparation of Autoclaved Aerated Concrete Using Copper Tailings and Blast Furnace Slag*, Construction and Building Materials, Elsevier, 27(1), 1–5, February 2012.

Memari, A. M., Lepage, A., and Setthachayanon, J., *An Experimental Study of Autoclaved Aerated Concrete Lintels Strengthened with Externally Bonded Glass FRP*, Journal of Reinforced Plastics and Composites, Sage Publications, 29(22), 3322–3337, November 2010.

Milanesi, R. R., Morandi, P., and Magenes, G., *Local Effects on RC Frames Induced by AAC Masonry Infills Through FEM Simulation of In-Plane Tests*, Bulletin of Earthquake Engineering, Springer, 16(9), 4053–4080, September 2018.

Mousa, M. A., and Uddin, N., *Experimental and Analytical Study of Carbon Fiber-Reinforced Polymer (FRP)/Autoclaved Aerated Concrete (AAC) Sandwich Panels*, Engineering Structures, Elsevier, 31(10), 2337–2344, October 2009.

Schwarz, S., Hanaor, A., and Yankelevsky, D. Z., *Experimental Response of Reinforced Concrete Frames with AAC Masonry Infill Walls to In-plane Cyclic Loading*, Structures, Elsevier, 3, 306–319, August 2015.

Tanner, J. E., Varela, J. L, Klingner, R. E., Brightman, M. J., and Cancino, U., *Seismic Testing of Autoclaved Aerated Concrete Shear Walls: A Comprehensive Review*, ACI Structural Journal, ACI, 102(3), 374-382, May-June 2005.

Tuncer, E., Binici, B., and Canbay, E., *Behavior and Design of FRP Bonded Autoclaved Aerated Concrete Beams*, Construction and Building Materials, Elsevier, 282, 122712, May 2021.

Varela, J. L., Tanner, J. E., and Klingner, R. E., *Development of Seismic Force Reduction and Displacement Amplification Factors for Autoclaved Aerated Concrete Structures*, Earthquake Spectra, Sage Publications, 22(1), 267–286, February 2006.